

The Self-Assembly Mechanism of Alkanethiols on Au(111)

G. E. Poirier* and E. D. Pylant†

The self-assembly mechanism of alkanethiol monolayers on the (111) surface of gold was discovered with the use of an ultrahigh-vacuum scanning tunneling microscope. Monolayer formation follows a two-step process that begins with condensation of low-density crystalline islands, characterized by surface-aligned molecular axes, from a lower density lattice-gas phase. At saturation coverage of this phase, the monolayer undergoes a phase transition to a denser phase by realignment of the molecular axes with the surface normal. These studies reveal the important role of molecule-substrate and molecule-molecule interactions in the self-assembly of these technologically important material systems.

Self-assembly of amphiphilic molecules into highly ordered monolayer films on metal surfaces has potential applications in biosensing (1), biomimetics (2), and corrosion inhibition (3). A specific amphiphile/substrate system that has received considerable attention recently is functionalized alkanethiols (HS(CH₂)_nX)(C_nX) self-assembled on Au(111) (4, 5). The interest in alkanethiol self-assembled monolayers (SAMs) stems from their stability and ease of preparation. Many studies have addressed their saturation-coverage equilibrium structure (5, 6), but relatively few have examined the mechanism of self-assembly.

The growth kinetics of SAMs have been studied using ellipsometry, contact angle measurements (7), surface acoustic wave devices (8), second-harmonic generation (9), near-edge x-ray absorption fine structure (10), and quartz crystal microbalances (11). These studies found that the growth rate is proportional to the number of unoccupied adsorption sites, in agreement with simple first-order Langmuir adsorption kinetics (8, 9, 11)

$$\frac{d\theta}{dt} = -k(1 - \theta) \quad (1)$$

where θ is the fraction of occupied sites, t is time, and k is a rate constant that contains the flux of thiol molecules to the surface and the sticking coefficient. All of the techniques used were spatially averaging and therefore left questions about the microscopic aspects of self-assembly unanswered. These questions include whether the monolayer assembles by nucleation and growth of islands or by a statistical "filling-in" mechanism, how the growing monolayer and the Au surface reconstruction interact, and what is the orientation of the alkyl chains during growth.

The goal of this report is to provide a detailed molecular-scale picture of the mechanism of self-assembly of alkanethiols onto Au(111). We accomplish this by using gas-phase transport of alkanethiols onto clean Au(111) single crystals in an ultrahigh-vacuum scanning tunneling microscope (STM) (12). We have studied growth of the methyl-terminated homologs $n = 5$ and 9 and the six-methylene unit homologs $X = \text{OH}$ and COOH . Our results highlight the importance of thiol-surface and thiol-thiol interactions in these self-assembling amphiphiles and may be generalizable to insoluble amphiphiles at the liquid-air interface.

The herringbone reconstructed surface of bare Au(111) (Fig. 1A) is characterized by a 4.3% uniaxial lateral contraction relative to the bulk layers (13). This contraction causes variations in registry between the surface and subsurface atomic layers such that the stacking arrangement alternates between normal ABC stacking and faulted ABA stacking with faulted and unfaulted regions delineated by rows of bridging Au atoms (14). These bridging rows are manifest in STM topographs as elevated ridges aligned with substrate $\langle 121 \rangle$ directions (15). Pairs of ridges form a ($\sqrt{3} \times 23$) surface unit cell that can adopt one of three orientational registries. To further reduce surface energy, the pairs form hyperdomains characterized by alternating 60° bends reminiscent of a herringbone pattern. Certain bend apices (arrows, Fig. 1A, inset) are more reactive than other sites because they contain surface-confined dislocations (15).

At very low surface coverage, the thiols adopt a lattice-gas phase that is characterized by a low areal density of rapidly diffusing surface-confined thiols. We cannot image the lattice gas directly because of the disparity between the time scales of molecular diffusion and STM data acquisition. When this lattice gas reaches a critical surface coverage, stable alkanethiol islands nucleate (circles, Fig. 1A, inset) (16). These islands grow in equilibrium with the lattice-

gas phase as inferred from three observations: there is a time-delay between initiation of dosing and appearance of stable islands, the herringbone reconstruction is altered before island nucleation, and the island boundaries fluctuate. Assuming a first-order phase transition, the lateral pressure of the lattice gas remains constant during the gas-solid coexistence.

Growth of Ni or Fe on Au(111) occurs by heterogeneous nucleation at the defect-ed herringbone elbows (arrows, Fig. 1A, inset), where a larger energy gain is realized (15, 17). In contrast, C₆OH SAM islands nucleate preferentially in regions of unfaulted Au stacking (circles, Fig. 1A, inset). If we assume a multimolecule critical island size and site-specific thiol binding (18), then it follows that there is an areal requirement for island nucleation on this periodically faulted surface (16). Because the ABC-stacked regions between alternate herringbone elbows present the largest unbroken area of unfaulted threefold hollow sites (15), they are the most likely place for critical island nucleation. Thus, the observed nucleation reflects dynamical rather than energetic aspects of self-assembly.

Exposing the surface to 200 Langmuirs (L) (1 L = 10⁻⁶ torr·s = 1.33 × 10⁻⁴ Pa·s) of C₆OH (Fig. 1B) results in the growth of islands exhibiting a striped pattern. Exposure to an additional 150 L results in formation and growth of additional striped-phase islands (Fig. 1C). The stripes are aligned with substrate $\langle 121 \rangle$ directions with a corrugation period of 5 Å along the rows and an interrow spacing of 22 Å (Fig. 2). This configuration is not consistent with the $c(4 \times 2)$ superlattice of a ($\sqrt{3} \times \sqrt{3}$)R30 lattice known to describe saturation coverage alkanethiols on Au(111) (6, 19). Instead, from the observed stripe orientation, corrugation period, and interrow spacing, we propose that the striped domains are composed of alkanethiolates with the sulfur atoms bound in next-nearest-neighbor threefold-hollow sites (18) and the molecular axes aligned with the surface plane (overlays, Fig. 2A). We refer to this proposed structure as solid₁. The STM topographs do not constitute unambiguous proof; however, helium diffraction measurements that show a correlation between interrow stripe period and alkanethiol chain length (20) support this model. Figure 2A does not allow us to assign a head-to-head or head-to-tail packing arrangement; however, if we assume the former, then the packing density is 60 Å² per molecule, whereas the latter implies 120 Å² per molecule. In either case, the surface molecular density of solid₁ is lower than the saturation density of 21.5 Å² per molecule (6, 19). These stripe-phase domains were not unique to gas-dosed C₆OH

National Institute of Standards and Technology, Gaithersburg, MD 20899, USA.

*To whom correspondence should be addressed.

†Permanent address: Department of Chemistry and Biochemistry, University of Texas, Austin, TX 78712, USA.

but also occurred, with subtle variations, for low-coverage liquid-phase-dosed molecules with other end groups (Fig. 2B).

Solid₁ island growth is accompanied by changes in the herringbone reconstruction. The natural herringbone elbow period of bare Au(111) is about 250 Å (Fig. 1A), whereas a compressed elbow period of 130 Å is observed for the partially covered surface (Fig. 1B). We attribute this phenomenon to lateral expulsion of elbows from regions of nascent island growth and compression of the elbows into denuded regions. Annihilation of the surface dislocation at the herringbone elbows apparently has a higher activation barrier than does lateral sliding of the entire dislocation across the surface. This compression of elbow defects persists until the compressed-elbow strain field exceeds the activation barrier for elbow annihilation.

The islands are elongated parallel to hy-

perdomain ridges and the island boundaries conform to the herringbone turns (Fig. 1, C and D). Although island growth parallel to hyperdomain ridges proceeds by lateral expulsion and compression of the herringbone elbows, growth perpendicular to the ridges must occur by annihilation or compression of the herringbone ridges. Apparently, the herringbone ridges are less compressible than the elbows, and this leads to the observed shape anisotropy and the conformal island boundaries.

Besides the shape anisotropy, solid₁ also has an orientational preference. Although solid₁ may adopt one of three symmetry-equivalent $\langle 121 \rangle$ orientations, comparison of Fig. 1A with 1D and 1E reveals a dominance of striped-phase domains oriented perpendicular to the preexisting hyperdomain ridges. This orientational preference is evident even for islands at the critical nucleation size (Fig. 1A, inset). We attribute

this preference to a break in the nucleation-site symmetry by the herringbone ridges.

Figures 1 and 2 establish that the SAM islands nucleate preferentially on unfaulted Au stacking domains at certain turns of the herringbone reconstruction, that the reconstruction is lifted by the self-assembly process, and that this lifting occurs locally with lateral expulsion of herringbone elbows. The appearance of one discrete crystalline phase is suggestive of a first-order, lattice-gas-to-solid₁ phase transition.

Lateral growth of solid₁ islands results in concomitant appearance of depressions (dark features, Fig. 1, C and D). The features, 2.5 Å in depth, are islands of Au atom vacancies (3, 21). In STM topograph sequences, we directly observed their formation in real time. In contrast to the SAM islands, the vacancy islands nucleate preferentially at elbows of the herringbone reconstruction, sites that also act as the locus

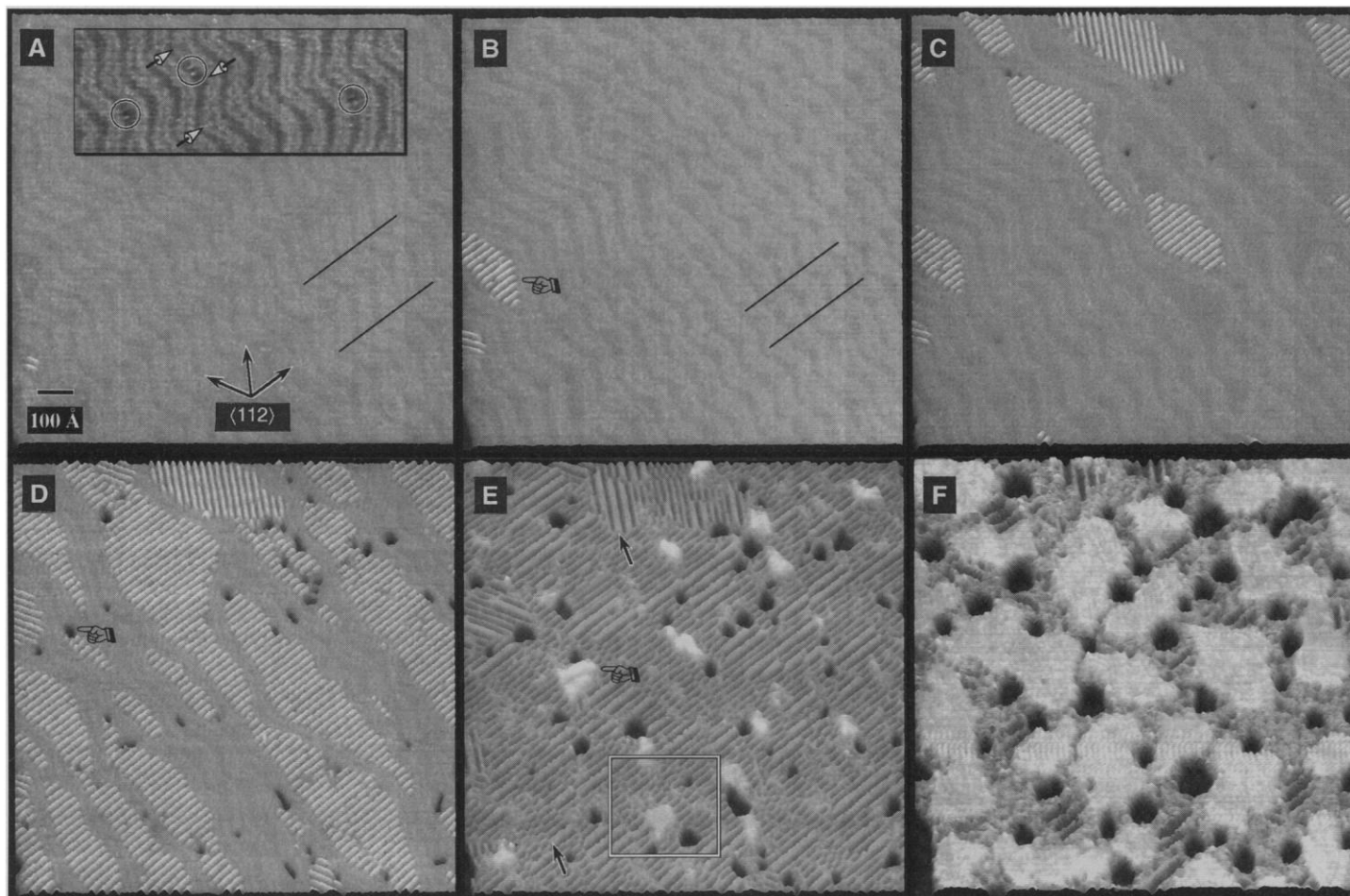


Fig. 1. Constant-current STM topographs showing the evolution of the reconstructed Au(111) surface during gas-phase transport of mercaptohexanol. Each frame was acquired in nominally the same surface region with a frame-to-frame lateral drift of less than 100 Å. **(A)** Bare surface (0 L) exhibits herringbone reconstruction. Parallel lines highlight native elbow periodicity; the small island in the lower left is residual contamination. (Inset) Surface exposed to 3 L. Three stable islands (circled) nucleate between herringbone double rows at certain bends in the reconstructed surface but do not nucleate at the surface dislocation site of the herringbone reconstruction (arrows). **(B)** Growth of striped-phase islands (pointing

finger) after 200 L. Parallel lines highlight compressed herringbone periodicity. **(C)** Continued striped-phase island growth displaces herringbone elbows after 350 L. **(D)** Au vacancy islands one atom deep (pointing finger) nucleate preferentially at elbows of herringbone hyperdomains after 600 L. **(E)** The second solid phase (pointing finger) nucleates after 1000 L, just above saturation coverage of the striped phase. Arrows indicate doubled striped-phase periodicity (upper) and antiphase boundaries (lower). A higher resolution topograph was acquired from the region indicated by the rectangle (Fig. 3). **(F)** Above 2500 L, the second phase grows at the expense of the striped phase until saturation.

of nucleation in Ni and Fe heteroepitaxy (15, 17).

Continued exposure of the surface to C_6OH vapor results in saturation of $solid_1$. Just above saturation of $solid_1$, elevated, corrugated islands appear (Figs. 1E and 3A). If each bright feature in these corrugated, commensurate, elevated islands is attributed to an individual thiolate, then these islands have a packing density of 21.5 \AA^2 per molecule (22). This packing density is identical to that of saturation-coverage SAMs of methyl-terminated alkanethiols (6, 19) and can only be achieved if the alkyl chains are oriented upright. Therefore, we attribute these features to islands of

the densest packed thiolate, in which the molecular axes are directed along the surface normal. We refer to this denser phase as $solid_2$.

$Solid_2$ islands appear only after saturation of $solid_1$, and they nucleate preferentially at $solid_1$ domain boundaries. This suggests that $solid_2$ nucleation is not limited by the adsorption kinetics but rather arises from lateral interactions in $solid_1$; that is, it is a phase transition driven by lateral pressure. Simultaneous with the nucleation of $solid_2$ islands, antiphase boundaries and regions with a larger stripe period form (arrows, Fig. 1E). Nevertheless, at the coverage indicated in Fig. 1E, discrete surface-aligned and surface-normal-aligned phases coexist.

According to the cross-sectional profile (Fig. 3B), $solid_2$ islands exhibit an apparent height of 0.8 \AA relative to $solid_1$, which itself has an apparent height of 1 \AA relative to the Au surface. Thus, the apparent height of $solid_2$ is significantly less than the C_6OH van der Waals length of $\approx 10 \text{ \AA}$, suggesting that the alkyl chains contribute minimally to the tunneling current, if at all. This is not unexpected, because the hydrocarbon chains have no electronic state density close to the Fermi level (23).

Figure 4 schematically summarizes the proposed self-assembly mechanism. With increasing coverage, the thiol molecules sequentially adopt a lattice-gas phase, a low-

density solid phase, and a higher density solid phase. Both solid phases are commensurate, differing mainly in the orientation of the chains. This same growth scheme was observed, with minor variations, for gas-phase-dosed C_6COOH , C_5CH_3 , and C_9CH_3 and for solution-phase-dosed C_9CH_3 ; thus, the mechanism appears to be a general model. The principal variation that we observe is that thiols with less intermolecular interaction, such as short-chain, methyl-terminated alkanethiols, exhibit a lattice-gas phase that persists to higher lateral pressure before nucleation of $solid_1$ islands and the phase transition from $solid_1$ to $solid_2$ occurs by way of several intermediate-density surface-aligned phases.

Similar two-step growth mechanisms have been seen for Langmuir-Blodgett amphiphile monolayers confined to the air-liquid interface in Langmuir-Blodgett troughs (24). In these systems, the phase transitions are manifest as discontinuities in lateral-pressure versus molecular-area isotherms. Since the early work by Adam (25), the precise order of the transitions—first-order or continuous—and the physical state of the phases—two-dimensional gas, liquid, or solid—have been controversial (26). This is due in part to the difficulty of direct determinations on liquid-confined phases. In our study, we examined amphiphile monolayer growth at a vacuum-crystal interface. Although growth on a liquid phase is expected to deviate fundamentally from that on a crystalline phase, the two-step growth mode presented here may be useful

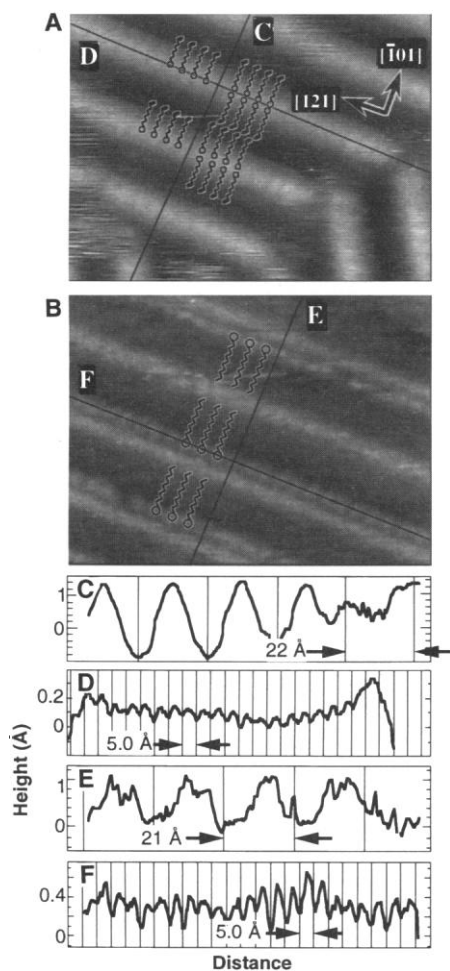


Fig. 2. Molecular-resolution, constant-current STM topographs of striped-phase alkanethiols on Au(111). (A) Low-coverage surface prepared by exposing substrate to 1000 L of mercaptohexanol vapor. Head-to-tail (left) and head-to-head (right) packing geometries are suggested by overlays. (B) Low-coverage surface prepared by incubating crystal in a $4.5 \mu\text{M}$ solution of decanethiol in ethanol for 50 s. (C through F) Cross-sectional profiles from corresponding traces in (A) and (B). Periodicities parallel and perpendicular to corrugated rows are consistent with a binding geometry in which molecular axes are aligned with the surface plane.

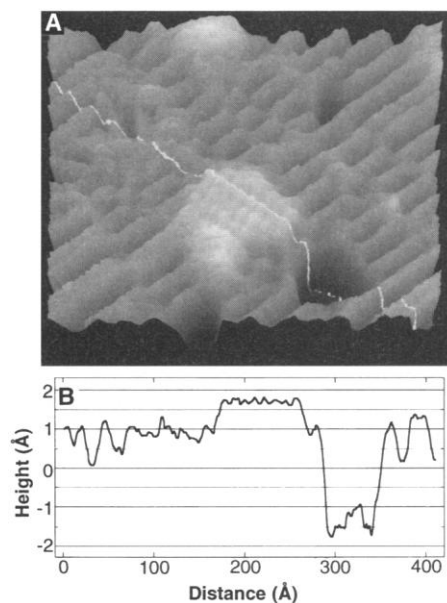


Fig. 3. (A) Molecular-resolution, constant-current STM topograph corresponding to the rectangle in Fig. 1E. The bright feature shows corrugation consistent with saturation-density molecular packing. (B) Cross-sectional profile corresponding to highlighted line in (A) showing an apparent height of 0.8 \AA for the bright feature with respect to the striped-phase and a depth of 2.5 \AA for the Au vacancy island.

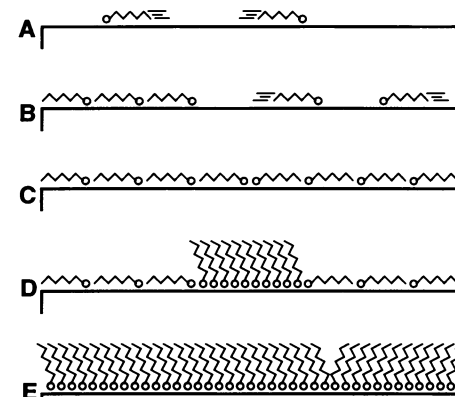


Fig. 4. Schematic of self-assembly mechanism for alkanethiols on Au(111). (A) Thiols adopt the highly mobile lattice-gas phase at very low coverage. (B) Above a critical value of surface coverage, striped-phase islands, characterized by surface-aligned molecular axes, nucleate heterogeneously and grow in equilibrium with a constant-pressure lattice gas. (C) Surface reaches saturation coverage of striped phase. (D) Surface undergoes lateral-pressure-induced solid-solid phase transition by nucleation of high-density islands at striped-phase domain boundaries. (E) High-density islands grow at the expense of the striped phase until the surface reaches saturation.

as a general guide to amphiphile monolayer assembly. In addition to improving our basic knowledge of molecular self-assembly, these results may be useful in guiding efforts to grow more highly ordered films and self-assembled supramolecular architectures.

REFERENCES AND NOTES

1. L. Haussling, W. Knoll, H. Ringsdorf, F.-J. Schmitt, J. Yang, *Makromol. Chem. Macromol. Symp.* **46**, 145 (1991).
2. P. A. DiMilla *et al.*, *J. Am. Chem. Soc.* **116**, 2225 (1994).
3. O. Chailapakul, L. Sun, C. Xu, R. M. Crooks, *ibid.* **115**, 12459 (1993).
4. L. C. F. Blackman and M. J. S. Dewar, *J. Chem. Soc.* **1957**, 162 (1957).
5. L. H. Dubois and R. G. Nuzzo, *Annu. Rev. Phys. Chem.* **43**, 437 (1992).
6. N. Camillone, C. E. D. Chidsey, G.-y. Liu, G. Scoles, *J. Chem. Phys.* **98**, 3503 (1993); G. E. Poirier and M. J. Tarlov, *Langmuir* **10**, 2853 (1994).
7. C. D. Bain and G. M. Whitesides, *J. Am. Chem. Soc.* **111**, 7164 (1989).
8. R. C. Thomas, L. Sun, R. M. Crooks, A. J. Ricco, *Langmuir* **7**, 620 (1991).
9. M. Buck, M. Grunze, F. Eisert, J. Fischer, F. Trager, *J. Vac. Sci. Technol. A* **10**, 926 (1992).
10. G. Hahner, C. Woll, M. Buck, M. Grunze, *Langmuir* **9**, 1955 (1993).
11. D. S. Karpovich and G. J. Blanchard, *ibid.* **10**, 3315 (1994).
12. Our measurements were performed in a multichamber ultrahigh-vacuum (UHV) surface-analysis system that has a base pressure of 3×10^{-8} Pa (2×10^{-10} torr) and is equipped with a rapid-entry load lock. Single crystals of Au(111) were cleaned by sputtering and annealing to 500° to 600°C for 10 min. After this preparation, x-ray photoelectron spectroscopy revealed a contamination-free surface and STM topographs showed the herringbone reconstruction characteristic of clean Au(111). These topographs were used to establish the sample's crystallographic orientation with respect to the STM scan direction. For gas-phase deposition, the molecules were stored in an ambient-temperature, blackened-glass vial attached to the UHV chamber by a variable-aperture leak valve. We purified the neat alkanethiols using freeze-pump-thaw cycles and confirmed the purity using in situ quadrupole mass spectrometry. Dosing pressures were typically 1×10^{-5} Pa (1×10^{-7} torr). For liquid-phase deposition, 4.5 μ M solutions of C_nX in ethanol were prepared, and the coverage was controlled by variation of the incubation time. We prepared the STM tips from single-crystal tungsten wire using a dc etch. All STM imaging was done at room temperature in constant-current mode. The tunneling-current set point was fixed between 5 and 100 pA, and the bias voltage was set between \pm (200 to 400) mV.
13. A. R. Sandy, S. G. J. Mochrie, D. M. Zehner, K. G. Huang, D. Gibbs, *Phys. Rev. B* **43**, 4667 (1991).
14. C. Woll, S. Chiang, R. J. Wilson, P. H. Lippel, *ibid.* **39**, 7988 (1989).
15. D. D. Chambliss, R. J. Wilson, S. Chiang, *J. Vac. Sci. Technol. B* **9**, 933 (1991).
16. M. Zinke-Allmang, L. C. Feldman, M. H. Grabow, *Surf. Sci. Rep.* **16**, 378 (1992).
17. J. A. Stroschio, D. T. Pierce, R. A. Dragoset, P. N. First, *J. Vac. Sci. Technol. A* **10**, 1981 (1992).
18. H. Sellers, A. Ulman, Y. Shnidman, J. E. Eilers, *J. Am. Chem. Soc.* **70**, 2447 (1993).
19. P. Fenter, A. Eberhardt, P. Eisenberger, *Science* **266**, 1216 (1994).
20. N. Camillone, T. Y. B. Leung, P. Schwartz, P. Eisenberger, G. Scoles, *Langmuir*, in press.
21. K. Edinger, A. Golzhauser, K. Demota, C. Woll, M. Grunze, *Langmuir* **9**, 4 (1993); G. E. Poirier and M. J. Tarlov, *J. Phys. Chem.* **99**, 10966 (1995).
22. G. E. Poirier, E. D. Pylant, J. M. White, *J. Chem. Phys.*, in press.
23. C. Zubragel *et al.*, *Chem. Phys. Lett.* **219**, 127

- (1994); A. Karpfen, *J. Chem. Phys.* **75**, 238 (1981).
24. W. D. Harkins and E. Boyd, *J. Phys. Chem.* **45**, 20 (1941).
25. N. K. Adam, *Proc. R. Soc. London Ser. A* **101**, 516 (1922).
26. N. R. Pallas and B. A. Pethica, *Langmuir* **1**, 509 (1985).
27. We gratefully acknowledge R. W. Ashton for provid-

ing purified mercaptohexanol and A. Eberhardt, R. E. Cavicchi, P. Eisenberger, G. Scoles, and J. M. White for helpful discussions. E.D.P. gratefully acknowledges financial support from NSF under the auspices of the Summer Internship Program, grant NSF CHE 9391640.

20 December 1995; accepted 7 March 1996

Dynamic Ocean-Atmosphere Coupling: A Thermostat for the Tropics

De-Zheng Sun* and Zhengyu Liu

The ocean currents connecting the western tropical Pacific Ocean with the eastern tropical Pacific Ocean are driven by surface winds. The surface winds are in turn driven by the sea-surface temperature (SST) differences between these two regions. This dynamic coupling between the atmosphere and ocean may limit the SST in the tropical Pacific Ocean to below 305 kelvin even in the absence of cloud feedbacks.

Records of past climates and observations of the interannual fluctuations about the present climate suggest that the maximum tropical SST is somehow limited to below 305 K (1, 2). Ramanathan and Collins (3) hypothesized that the tropical Pacific SST is mainly regulated by a negative feedback from cirrus clouds, a controversial (4, 5) proposal they referred to as the "thermostat hypothesis." In this report, we propose an alternative thermostat for the SST in the tropical Pacific Ocean: the dynamic coupling between the atmosphere and ocean. The ocean currents that connect the western Pacific Ocean with the eastern Pacific Ocean are driven by surface winds. Surface winds are in turn driven by the SST differences between these two regions (6). This dynamic coupling plays a central role in the El Niño–Southern Oscillation phenomena (2, 7), but its importance for the mean tropical climate has been less clear.

To illustrate the mechanism by which the dynamic ocean-atmosphere coupling regulates the tropical SST, we consider a three-box model for the tropical Pacific Ocean coupled with a simple atmosphere (Fig. 1). The surface Pacific Ocean over the equatorial region is represented by two boxes with temperatures T_1 and T_2 . The two boxes are assumed to have the same volume. The subsurface ocean is represented by another box with temperature T_c . The ocean currents are driven by surface winds. Using T_e to represent the radiative-convective equilibrium temperature, the temperature that the surface ocean would attain in the absence of the ocean currents, and c to represent the reciprocal of the time scale for

the radiative-convective processes, we can write the heat budget of the two surface boxes over time t as

$$\frac{dT_1}{dt} = c(T_e - T_1) + q(T_2 - T_1) \quad (1)$$

$$\frac{dT_2}{dt} = c(T_e - T_2) + q(T_c - T_2) \quad (2)$$

with q given by

$$q = \alpha(T_1 - T_2) \quad (3)$$

where α is a constant related to the eddy-damping time scale in the atmospheric boundary layer and in the mixed layer of the ocean. The first term on the right side of Eqs. 1 and 2 is the local heat exchange with the atmosphere, and the second term is the advection of heat by the ocean currents. In deriving Eq. 3, we have assumed that the strength of the ocean cur-

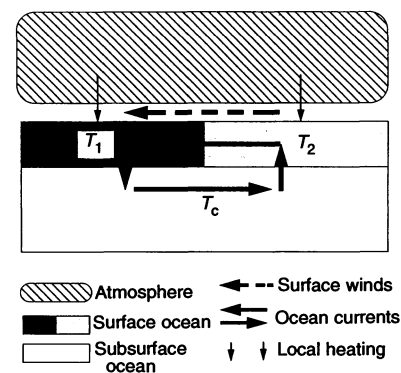


Fig. 1. A schematic diagram for the coupled model. The east-west surface current is the frictional flow driven by the east-west surface winds, and the return flow may be largely considered as the equatorial undercurrent. The east-west surface winds also drive a meridional cell that connects the equatorial subsurface ocean to the extratropical ocean (11).

D.-Z. Sun, National Center for Atmospheric Research, Boulder, CO 80307, USA.
Z. Liu, Department of Atmospheric and Oceanic Sciences, University of Wisconsin, Madison, WI 53706, USA.

*To whom correspondence should be addressed.